Supporting Informations

A Highly Conducting Tetrathiafulvalene-Tetracarboxylate Based Dysprosium(III) 2D Metal-Organic Framework with Single Molecule Magnet Behavior

Fabio Manna,[abc] Mariangela Oggianu,[ac] Pascale Auban-Senzier,[d] Ghenadie Novitchi,[e] Enric Canadell,[f] Maria Laura Mercuri*[ac] and Narcis Avarvari*[b]

[a] Dipartimento di Scienze Chimiche e Geologiche, Università degli Studi di Cagliari, I-09042 Monserrato, Italy. E-mail: mercuri@unica.it

[b] Univ Angers, CNRS, MOLTECH-ANJOU, SFR MATRIX, F-49000 Angers, France. E-mail: narcis.avarvari@univ-angers.fr

[c] INSTM, Via Giuseppe Giusti, 9, 50121 Firenze, Italy

[d] Université Paris-Saclay, CNRS, UMR 8502, Laboratoire de Physique des Solides, 91405 Orsay, France

[e] Laboratoire National des Champs Magnétiques Intenses, UPR CNRS 3228, Université Grenoble-Alpes, B.P. 166, 38042 Grenoble Cedex 9, France

[f] Institut de Ciència de Materials de Barcelona, ICMAB-CSIC, Campus de la UAB, 08193 Bellaterra, Spain, and Royal Academy of Sciences and Arts of Barcelona, Chemistry Section, La Rambla 115, 08002 Barcelona, Spain

Contents

Crystal Structure

Table S1. Selected distances (Å) and angles (deg)			
Dy-O_{COO-}		Dy-O_{H2O}	
Dy1-O3	2.323(4)	Dy1-O21	2.367(5)
Dy1-O9	2.283(5)	Dy1-O23	2.392(3)
Dy1-O2	2.526(5)	Dy1-O22	2.461(5)
Dy1-O1'	2.493(4)		
Dy1-O1	2.442(3)		
Dy1-O11	2.415(5)		
Dy2-O15	2.365(3)	Dy2-O26	2.387(4)
Dy2-O13	2.322(4)	Dy2-O27	2.361(5)
Dy2-O5	2.287(5)	Dy2-O25	2.405(5)
Dy2-O7	2.286(5)	Dy2-O24	2.376(5)
Dy3-O14	2.354(5)	Dy3-O30	2.402(5)
Dy3-O19	2.303(4)	Dy3-O29	2.470(3)
Dy3-O17	2.290(5)	Dy3-O31	2.394(4)
Dy3-O4	2.306(4)	Dy3-O28	2.447(4)
Selected angle			
Dy2-Dy3-Dy1	161.24(1)		
Dy3-Dy1-Dy1'	115.09(1)		
Dy1-O1-Dy1'	112.4(1)		

Symmetry code: (‘) 1-x,1-y,1-z		
Shape parameters calculated (SHAPE 2.1)		
Dy1		
Muffin (Cs)	**MFF-9**	**7.547**
Spherical capped square antiprism (C4v)	CSAPR-9	7.875
Spherical tricapped trigonal prism (D3h)	TCTPR-9	7.965
Dy2		
Biaugmented trigonal prism J50 (C2v)	**JBTPR-8**	**5.600**
Snub diphenoid J84 (D2d)	JSD-8	6.535
Biaugmented trigonal prism (C2v)	BTPR-8	6.538
Dy3		
Snub diphenoid J84 (D2d)	**JSD-8**	**5.466**
Biaugmented trigonal prism J50 (C2v)	JBTPR-8	6.407
BTPR-8	BTPR-8	7.814

Table S2. Contact distances < 7 Å for Dy^{III}	
interclusters	
Dy2···Dy3	5.6926(6)
Dy3···Dy1	5.1990(5)
Dy1···Dy1$^{(i)}$	4.1003(5)
intralayers	
Dy1···Dy3$^{(ii)}$	6.4200(7)
interlayers	
Dy2···Dy3$^{(III)}$	6.1672(7)
Dy2···Dy1$^{(IV)}$	6.4840(6)
Dy2···Dy2$^{(V)}$	6.1437(6)
Symmetry codes: (I) 1-x,1-y,1-z; (II)2-x,1-y,1-z, (III); x,y,1+z; (IV) x,-1+y,z; (V) 2-x,-y,2-z.	

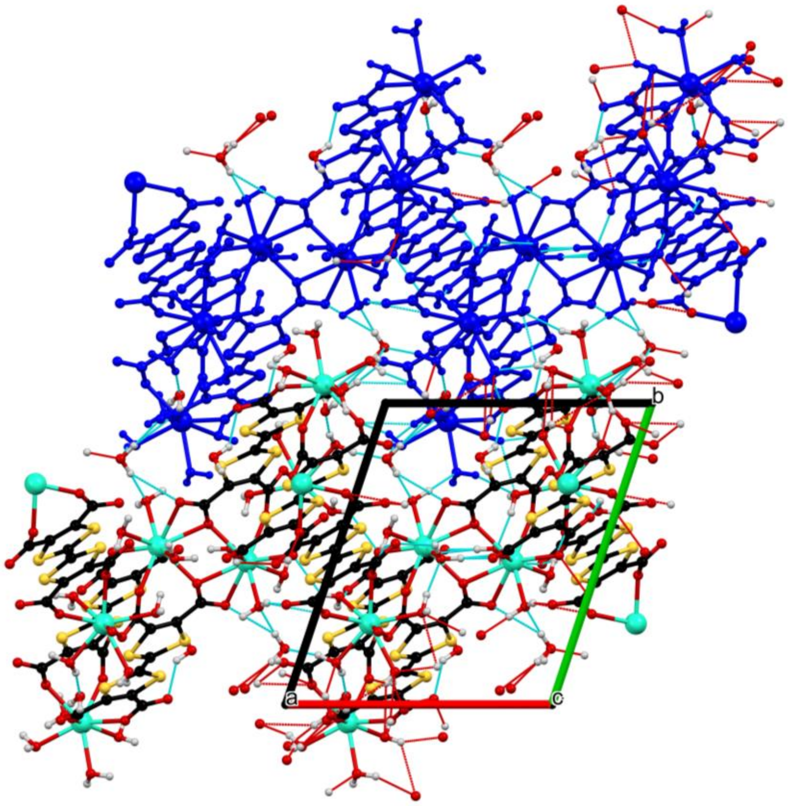

Figure S1. H-bond interaction within two different layers.

Table S3. Calculated parameters with Pore Analyser in Mercury		
Parameter	**Result**	**Unit**
System Volume	2670.61	Å³
System Mass	3253.15	g/mol
System Density	2.023	g/cm³
Total surface area	109.47	Å²
Total surface area per volume	409.9	m²/cm³
Total surface area per mass	202.65	m²/g
Network-accessible surface area	109.47	Å²
Network-accessible surface area per volume	409.9	m²/cm³
Network-accessible surface area per mass	202.65	m²/g
Total helium volume	712.72	Å³
Total helium volume	0.132	cm³/g
Total geometric volume	991.388	Å³
Total geometric volume	0.184	cm³/g
Network-accessible helium volume	712.075	Å³
Network-accessible helium volume	0.132	cm³/g
Network-accessible geometric volume	989.354	Å³
Network-accessible geometric volume	0.183	cm³/g
Pore limiting diameter	4.16	Å
Maximum pore diameter	5.54	Å

Pore and Thermal Analysis

a)

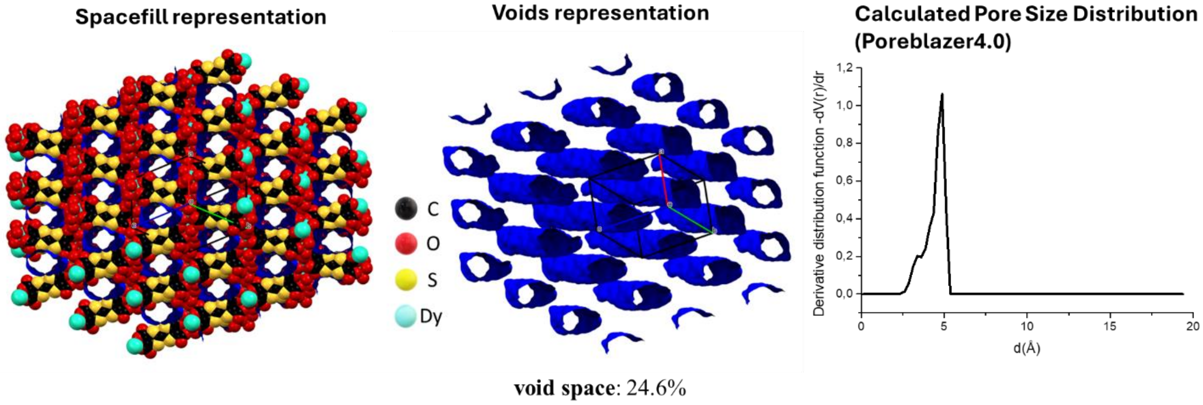

b)

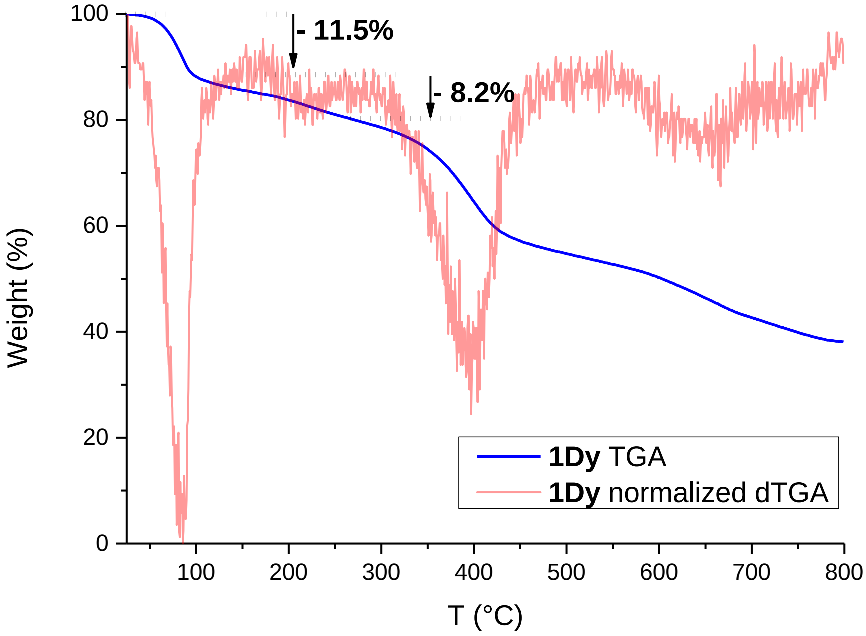

Figure S2. a) Sphere packing representation of the structure and the voids (in blue), left, and 1D voids representation, right. Pore size distribution calculated with Poreblazer4.0. b) Thermogram (blue) and dTGA normalized from 0 to 100 (red) for **1Dy** with weight loss highlighted.

Table S4. TTF bond distances* (Å) for reference compounds							
	a	b	c	d	δ	ρ	Ref.
MIL-132K	1.340	1.768	1.747	1.360	0.815	0	[1]
MIL-133K	1.353	1.756	1.751	1.353	0.801	0	[1]
MIL-135K	1.401	1.720	1.729	1.359	0.689	1	[1]
$Co(H_2O)_6(TTFTC)H_2\cdot 2H_2O$	1.335	1.752	1.745	1.356	0.806	0	[2]
$[Zn(bipy)_2(H_2O)_4][Zn(TTFTC)(H_2O)_2]$	1.327	1.759	1.750	1.356	0.845	0	[2]
$[Fe(bipy)_2(H_2O)_4][Fe(TTFTC)(H_2O)_2]$	1.328	1.761	1.747	1.336	0.836	0	[2]
$[Co_2(\mu_2\text{-}OH_2)_2(H_2O)_8](H_2TTFTC)_2$	1.344	1.744	1.746	1.345	0.812	0	[3]
$\{(MV)(L)[Na_2(H_2O)_8]\cdot 4H_2O\}_n$	1.338	1.759	1.754	1.334	0.854	0	[4]
$\{(MV)[Mn(L)(H_2O)_2]\cdot 2H_2O\}_n$	1.312	1.765	1.775	1.321	0.895	0	[4]
1-$\{(MV)[Mn(L)(H_2O)_2]\}_n$	1.342	1.759	1.765	1.332	0.851	0	[4]
2-$\{(MV)[Mn(L)(H_2O)_2]\}_n$	1.342	1.770	1.778	1.331	0.875	0	[4]
$([Na_4(TTFTC)(H_2O)_2]\cdot 0.5H_2O)$[47]	1.342	1.759	1.747	1.335	0.829	0	[5]
$[Rb_4(TTFTC)(H_2O)_3]\cdot H_2O$	1.332	1.762	1.757	1.336	0.851	0	[5]
1-$[Cs_4(TTFTC)(H_2O)_2]$	1.317	1.764	1.756	1.368	0.834	0	[5]
2-$[Cs_4(TTFTC)(H_2O)_2]$	1.317	1.770	1.758	1.340	0.870	0	[5]
*Mean distances value are reported for each TTF-five-member ring, labels 1 and 2 correspond to different ring for non-centrosymmetric TTF.							

Table S5. contacts S···S distances < 3,90 Å (in bold < 3,60 Å)					
interlayer		intralayer			
1		2		3	
S1···S4$^{(IV)}$	3.702(2)	S1···S5	3.858(2)	**S5···S10$^{(I)}$**	3.493(2)
S2···S3$^{(IV)}$	**3.559(2)**	S2···S6	3.654(2)	**S6···S9$^{(I)}$**	3.516(2)
S3···S4$^{(IV)}$	3.884(2)	S3···S7	3.834(2)	**S7···S9$^{(II)}$**	3.594(2)
		S4···S8	3.763(2)	**S8···S10$^{(II)}$**	3.506(2)
		S4···S6	3.814(2)	S8···S9$^{(III)}$	3.802(2)
Symmetry codes: (I) 2-x,1-y,1-z; (II) x, y,1+z; (III) 2-x,1-y,1-z; (IV) 1-x,-y,1-z					

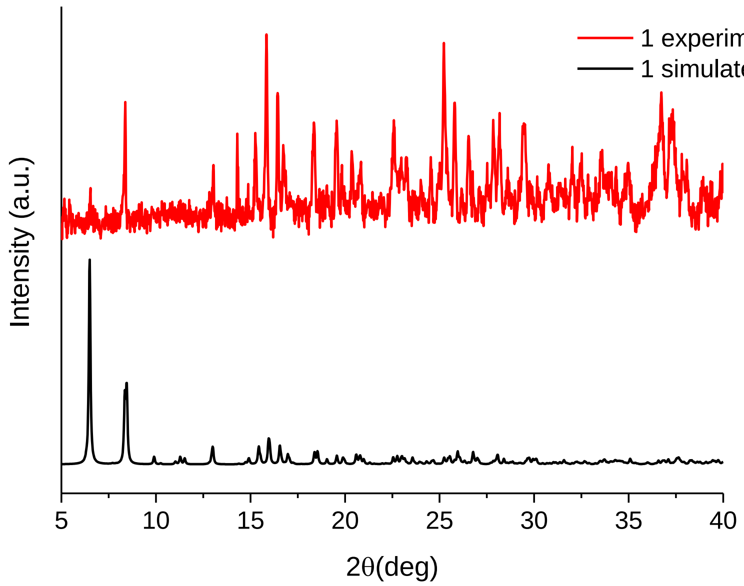

Figure S3. experimental (top, red) and calculated (bottom, black) PXRD pattern for 1-Dy.

Photophysical characterization

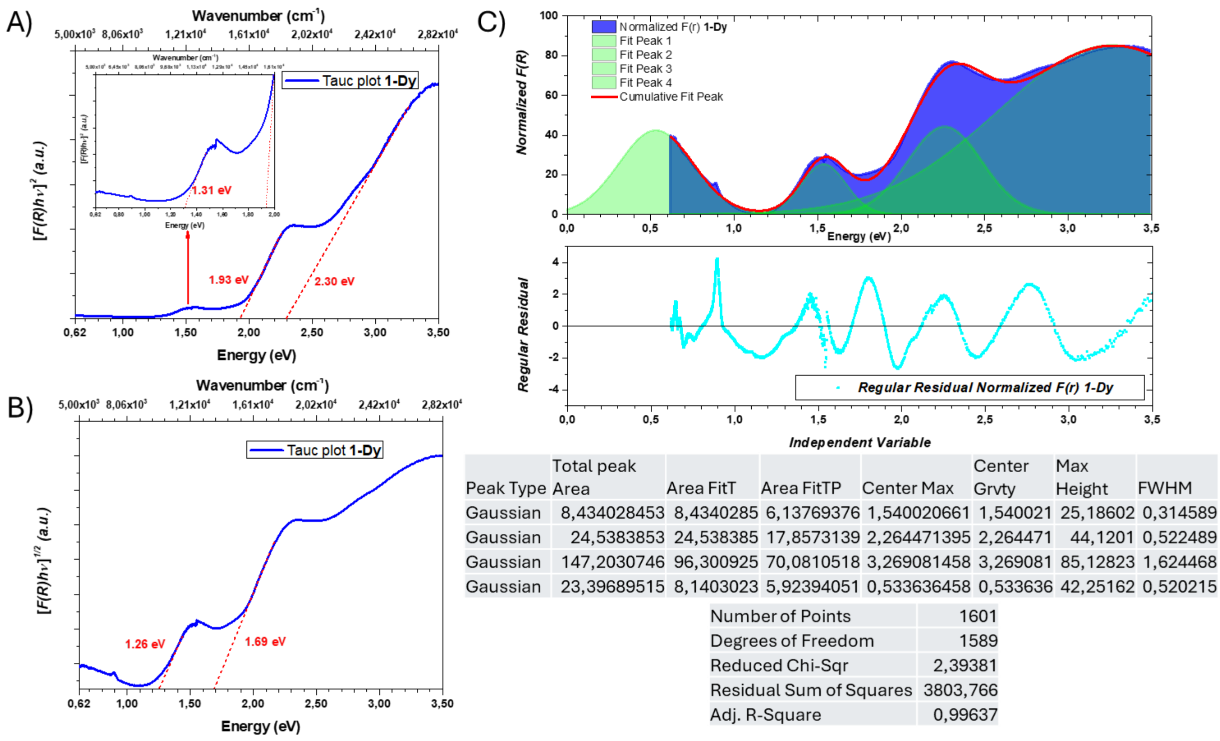

Peak Type	Total peak Area	Area FitT	Area FitTP	Center Max	Center Grvty	Max Height	FWHM
Gaussian	8,434028453	8,4340285	6,13769376	1,540020661	1,540021	25,18602	0,314589
Gaussian	24,5383853	24,538385	17,8573139	2,264471395	2,264471	44,1201	0,522489
Gaussian	147,2030746	96,300925	70,0810518	3,269081458	3,269081	85,12823	1,624468
Gaussian	23,39689515	8,1403023	5,92394051	0,533636458	0,533636	42,25162	0,520215

Number of Points	1601
Degrees of Freedom	1589
Reduced Chi-Sqr	2,39381
Residual Sum of Squares	3803,766
Adj. R-Square	0,99637

Figure S4. a) Direct and b) indirect band gaps optical determination trough Tauc plot. c) Gaussian fit with regular residual graphic and gaussian fit parameters calculated by Origin9.

Electron transport properties of TTF-MOFs

Table S6. Selected example for conductive TTF-MOFs.

Compound	σ_{rt}(S/cm)	Ea (eV)	Method	Ref.
Cd_2(TTFTB)	2.86×10^{-4}	0.293	2-probe SC	[6]
Zn_2(TTFTB)	3.95×10^{-6}		2-probe SC	[6]
Mn_2(TTFTB)	8.64×10^{-5}		2-probe SC	[6]
Co_2(TTFTB)	1.49×10^{-5}		2-probe SC	[6]
$La_4(TTFTB)_4$	2.5×10^{-6}	0.28	2-probe pellet	[7]
La(TTFTB)	9.0×10^{-7}	0.20	2-probe pellet	[7]
$La_4(TTFTB)_3$	1.0×10^{-9}	0.40	2-probe pellet	[7]
Dy(TTFTB)	3×10^{-7}		4-probe pellet	[8]
$Gd_3(TTFTB)_2$(OAc)(OH)	2.0×10^{-7}		4-probe pellet	[8]
$Tb_3(TTFTB)_2$(OAc)(OH)	1.5×10^{-6}		4-probe pellet	[8]
$Dy_3(TTFTB)_2$(OAc)(OH)	3.9×10^{-7}		4-probe pellet	[8]
$Ho_3(TTFTB)_2$(OAc)(OH)	6.7×10^{-6}		4-probe pellet	[8]
$Er_3(TTFTB)_2$(OAc)(OH)	7.4×10^{-6}		4-probe pellet	[8]
$Er_4(TTFTB)_3(I_3)_2$	2×10^{-8}		2-probe pellet	[9]
$Er_4(TTFTB)_3$	1×10^{-9}		2-probe pellet	[9]
$Tb_4(TTFTB)_3(I_3)_2$	4×10^{-8}		2-probe pellet	[9]
$Tb_4(TTFTB)_3$	1×10^{-8}		2-probe pellet	[9]
$Dy_4(TTFTB)_3(I_3)_2$	1×10^{-8}		2-probe pellet	[9]
$Dy_4(TTFTB)_3$	7×10^{-9}		2-probe pellet	[9]
$Ho_4(TTFTB)_3(I_3)_2$	8×10^{-9}		2-probe pellet	[9]
$Ho_4(TTFTB)_3$	1×10^{-9}		2-probe pellet	[9]
$Yb_6(TTFTB)_5$	9×10^{-7}		2-probe pellet	[10]
$Lu_6(TTFTB)_5$	3×10^{-7}		2-probe pellet	[10]
$\{[Gd_4(TTF\text{-}DC)_6(DMF)_4(H_2O)_2]\cdot 4DMF\}_n$	2.13×10^{-10}		2-probe pellet	[11]
$\{[Tb_4(TTF\text{-}DC)_6(DMF)_4(H_2O)_2]\cdot 4DMF\}_n$	1.54×10^{-10}		2-probe pellet	[11]
$\{[Dy_4(TTF\text{-}DC)_6(DMF)_4(H_2O)_2]\cdot 4DMF\}_n$	1.24×10^{-10}		2-probe pellet	[11]
$\{[Er_4(TTF\text{-}DC)_6(DMF)_4(H_2O)_2]\cdot 4DMF\}_n$	6.63×10^{-9}		2-probe pellet	[11]
$\{[Gd_4(TTF\text{-}DC)_4(DMF)_4(H_2O)_2(TTF^{\cdot+}\text{-}DC)_2](I_3^-)_2\}_n$	2.96×10^{-7}		2-probe pellet	[11]
$\{[Er_4(TTF\text{-}DC)_4(DMF)_4(H_2O)_2(TTF^{\cdot+}\text{-}DC)_2](I_3^-)_2\}_n$	9.88×10^{-7}		2-probe pellet	[11]

{[Tb_4(TTF-DC)$_4$(DMF)$_4$(H_2O)$_2$(TTF$^{\cdot+}$-DC)$_2$](I_3^-)$_2$}$_n$	1.28×10^{-6}		2-probe pellet	[11]
{[Dy_4(TTF-DC)$_4$(DMF)$_4$(H_2O)$_2$(TTF$^{\cdot+}$-DC)$_2$](I_3^-)$_2$}$_n$	2.19×10^{-6}		2-probe pellet	[11]
([Na_4(TTFTC)(H_2O)$_2$]·0.5H_2O)	3.4×10^{-5}	0.06	2-probe pellet	[5]
([K_4(TTFTC)(H_2O)$_2$]·2H_2O)	1.7×10^{-5}	0.18	2-probe pellet	[5]
([K_4(TTFTC)(H_2O)$_2$]·2H_2O)(ox)	6.3×10^{-5}	0.16	2-probe pellet	[5]
([Rb_4(TTFTC)(H_2O)$_3$]·H_2O)	1.5×10^{-5}	0.19	2-probe pellet	[5]
([Rb_4(TTFTC)(H_2O)$_3$]·H_2O)(ox)	4.1×10^{-5}	0.19	2-probe pellet	[5]
([Cs_4(TTFTC)(H_2O)$_2$])	1.3×10^{-7}		2-probe pellet	[5]
([Tb_6(mTTFTB)2.5(μ_3-OH)8(H_2O)$_2$(HCOO)$_2$]	1.8×10^{-8}		2-probe pellet	[12]
([Dy_6(mTTFTB)2.5(μ_3-OH)8(H_2O)$_2$(HCOO)$_2$]	3.0×10^{-8}		2-probe pellet	[12]
([Er_6(mTTFTB)2.5(μ_3-OH)8(H_2O)$_2$(HCOO)$_2$]	7.1×10^{-8}		2-probe pellet	[12]
[(CuCN)$_2$(TTF(py)$_4$)]	3.5×10^{-10}		2-probe pellet	[13]
[(CuCN)$_2$(TTF(py)$_4$)] (I_2 ox)	2.3×10^{-5}		2-probe pellet	[13]
[Cu(H_2TTFTB)(NH_2Me_2)]·2DMF·4H_2O	1.12×10^{-5}		Not specified	[14]
[Cu(H_2O)(H_2TTFTB)(NH_2Me_2)0.5]·2C_6H_{12}	1.17×10^{-5}		Not specified	[14]
Mn_4(TTFTB)$_4$(H_2O)7DMF	3.17×10^{-6}		2-probe pellet	[15]
Co_6(TTFTB)$_4$(H_2O)	1.66×10^{-7}		2-probe pellet	[15]
Co(H_2TTFTB)(H_2O)4DMF	$8.97 \times 1 0^{-9}$		2-probe pellet	[15]
(UO_2)$_4$(TTFTB)$_3$(DMA)$_4$(H2O)$_6$(DMF)$_8$	2.2×10^{-7}		4-probe pellet	[16]
[Zn(TTF(py)$_4$)(TCNQ$^{\bullet-}$)$_{1/2}$](TCNQ$^{\bullet-}$)$_{1/2}$(NO_3)·2CH_3OH	2.48×10^{-8}		2-probe pellet	[17]
[Cd(TTF(py)$_4$)(TCNQ$^{\bullet-}$)$_{1/2}$](TCNQ$^{\bullet-}$)$_{1/2}$(NO_3)·CH_2Cl_2	2.63×10^{-8}		2-probe pellet	[17]
[Cd(TTF(py)$_4$)(TCNQ$^{\bullet-}$)$_{1/2}$](I_3)(NO_3)$_{1/2}$·1/2(C_6H_{12}·CH_3OH)	2.16×10^{-7}		2-probe pellet	[17]
[Ni(py-TTF-py)(BPDC)]·2H_2O	8.0×10^{-11}		2-probe pellet	[18]
[Zn(py-TTF-py)(BPDC)]·2H_2O	4.1×10^{-12}		2-probe pellet	[18]
[Ni(py-TTF-py)(BPDC)]·2H_2O (I_2 ox)	2.5 × 10–5		2-probe pellet	[18]
[Zn(py-TTF-py)(BPDC)]·2H_2O (I_2 ox)	1.9×10^{-5}		2-probe pellet	[18]
[Fe(dca)$_2$][TTF(py)$_4$]0.5·0.5CH_2Cl_2}n	4.1×10^{-9}		2-probe pellet	[19]
{[Fe(dca)][TTF(py)$_4$]·ClO_4·CH_2Cl_2·2CH_3OH]}n	1.2×10^{-7}		2-probe pellet	[19]
[Fe(dca)$_2$][TTF(py)$_4$]$_{0.5}$·0.5CH_2Cl_2}n (I_2 ox)	1.3×10^{-6}		2-probe pellet	[19]
{[Fe(dca)][TTF(py)$_4$]·ClO_4·CH_2Cl_2·2CH_3OH]}n (I_2 ox)	7.6×10^{-5}		2-probe pellet	[19]
Zn_3(ExTTFTB)$_2$(H_2O)$_4$·6EtOH	3.02×10^{-10}		2-probe pellet	[20]

$Zn_3(ExTTFTB)_2(H_2O)_4 \cdot 6EtOH$ (I_2 ox)	3.18×10^{-6}		2-probe pellet	[20]
Zn_2(DPTTF)(TCPB)·3DMA	1×10^{-8}		2-probe pellet	[21]
Zn_2(DPTTF)(TCPB)·3DMA (I_2 ox)	5×10^{-7}		2-probe pellet	[21]
(BVDT-TTF-Py_4)($CdCl_2$)	$7–9 \times 10^{-10}$		2-probe SC	[22]
(BVDT-TTF-Py_4)($CdCl_2$)(I_3)	$4–6 \times 10^{-9}$		2-probe SC	[22]
$[Dy_6(TTFTC)_5(H_2O)_{22}]\cdot(H_2O)_{21}$	**1×10^{-3}**	**0.164**	4-probe SC & 2-probe SC	**This work**

Magnetic Properties

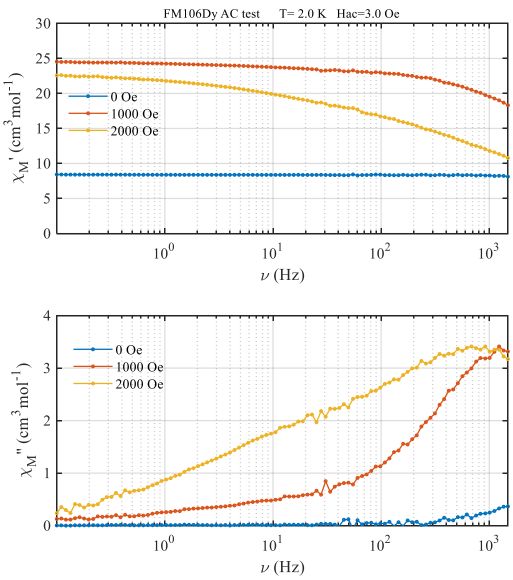

Figure S5. *ac* susceptibility of **1Dy** at 0.0, 1.0 and 2.0 kOe,

$$\chi'(\omega) = \chi_{S,tot} + \Delta\chi_1 \frac{1+(\omega\tau_1)^{1-\alpha_1}\sin\left(\frac{\pi\alpha_1}{2}\right)}{1+(\omega\tau_1)^{1-\alpha_1}\sin\left(\frac{\pi\alpha_1}{2}\right)+(\omega\tau_1)^{(2-2\alpha_1)}} + \Delta\chi_2 \frac{1+(\omega\tau_2)^{1-\alpha_2}\sin\left(\frac{\pi\alpha_2}{2}\right)}{1+(\omega\tau_2)^{1-\alpha_2}\sin\left(\frac{\pi\alpha_2}{2}\right)+(\omega\tau_2)^{(2-2\alpha_2)}} \quad \text{(eq-1)}$$

$$\chi''(\omega) = \Delta\chi_1 \frac{1+(\omega\tau_1)^{1-\alpha_1}\cos\left(\frac{\pi\alpha_1}{2}\right)}{1+(\omega\tau_1)^{1-\alpha_1}\sin\left(\frac{\pi\alpha_1}{2}\right)+(\omega\tau_1)^{(2-2\alpha_1)}} + \Delta\chi_2 \frac{1+(\omega\tau_2)^{1-\alpha_2}\cos\left(\frac{\pi\alpha_2}{2}\right)}{1+(\omega\tau_2)^{1-\alpha_2}\sin\left(\frac{\pi\alpha_2}{2}\right)+(\omega\tau_2)^{(2-2\alpha_2)}} \quad \text{(eq-2)}$$

Were $\omega = 2\pi$

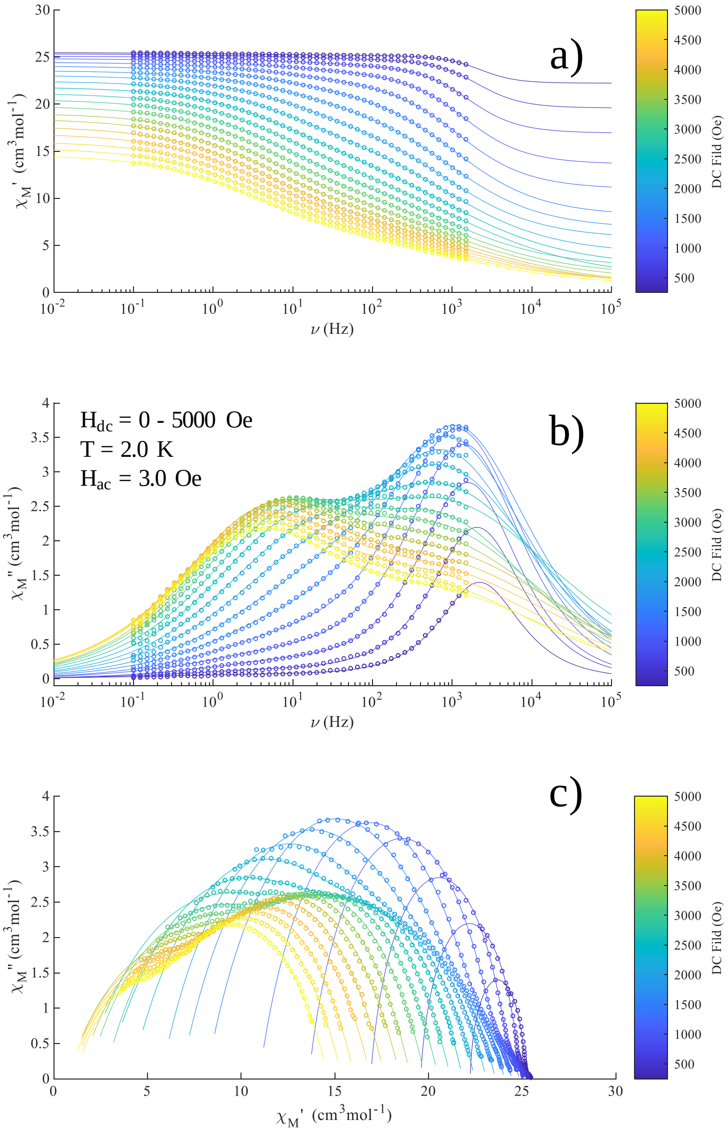

Figure S6. Field dependence of *ac* susceptibility a,b) (H_{ac}=3.0 Oe) and Cole-Cole plots(c) for **1** at indicated temperature and field. The solid lines represented the best fits according the generalized Debye model for two relaxation processes. (eq. 1, 2) see also **Figure S8**).

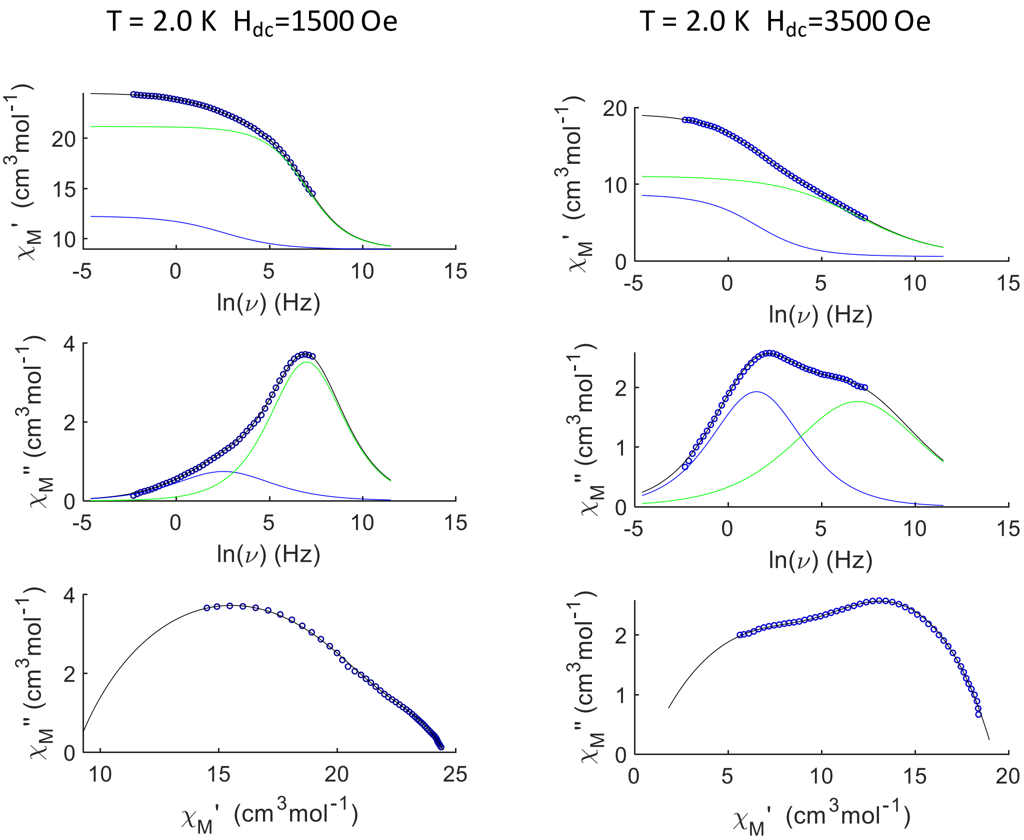

Figure S7. Example of AC susceptibility analysis for $[Dy_6(TTFTC)_5(H_2O)_{22}]\cdot(H_2O)_{21}$ (**1**) using the extended Debye model for two relaxation processes at H_{dc}=1500 Oe (left) and H_{dc}=3500 Oe (right). The contributions of the two relaxation processes are depicted in blue and green.

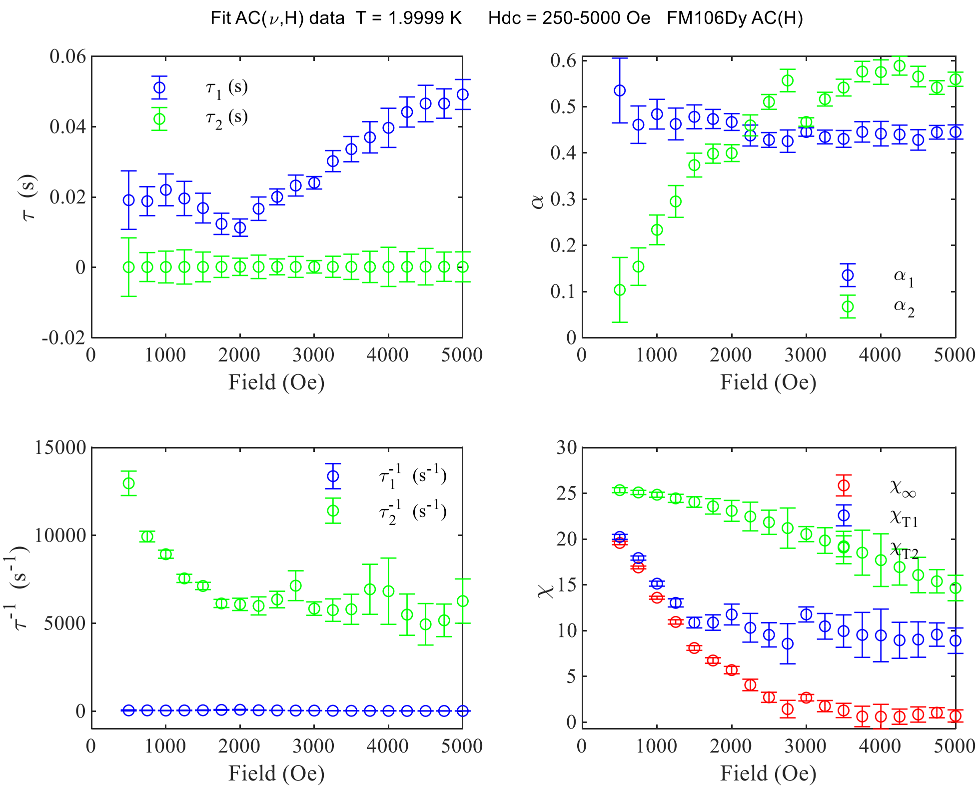

Figure S8. Graphical representation of variable parameters deduced from the best fits of the *ac* susceptibility of **1** collected with a 3.0 Oe *ac* field oscillating under different *dc* fields using the generalized Debye model for two relaxation processes. (See **Figure S6**).

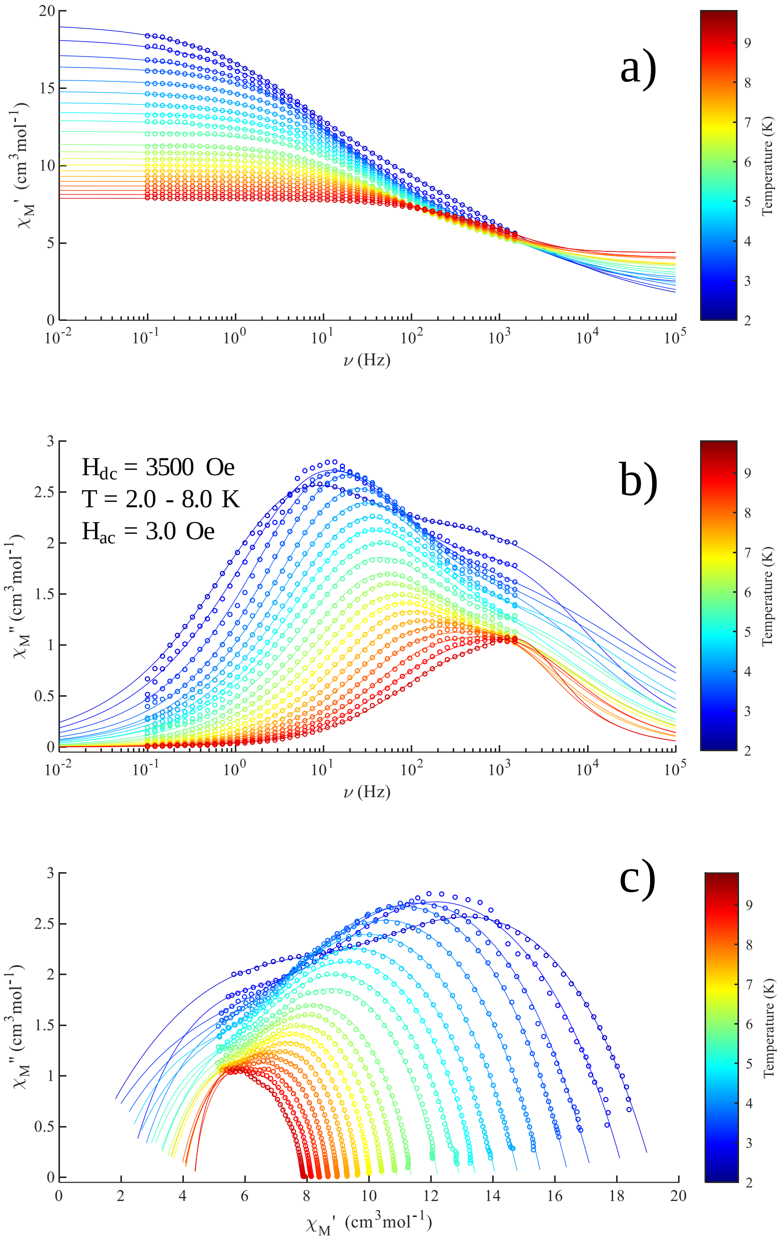

Figure S9. Temperature dependence of *ac* susceptibility a,b) (H_{ac}=3.0 Oe) and Cole-Cole plots (c) for **1** at indicated temperature and field. The solid lines represented the best fits according to the generalized Debye model for two relaxation processes. (eq. 1, 2) see also **Figure S10**)

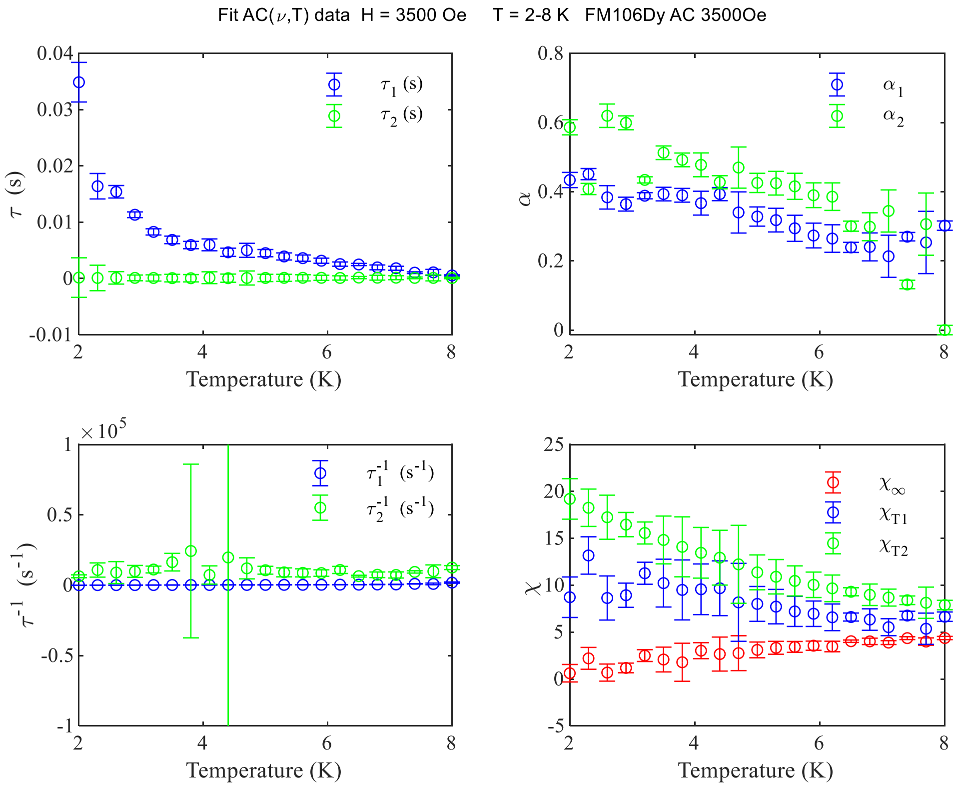

Figure S10. Graphical representation of variable parameters deduced from the best fits of the *ac* susceptibility of **1** collected under 1.5 kOe static field at deferent temperatures using the generalized Debye model for two relaxation processes. (See **Figure S9**).

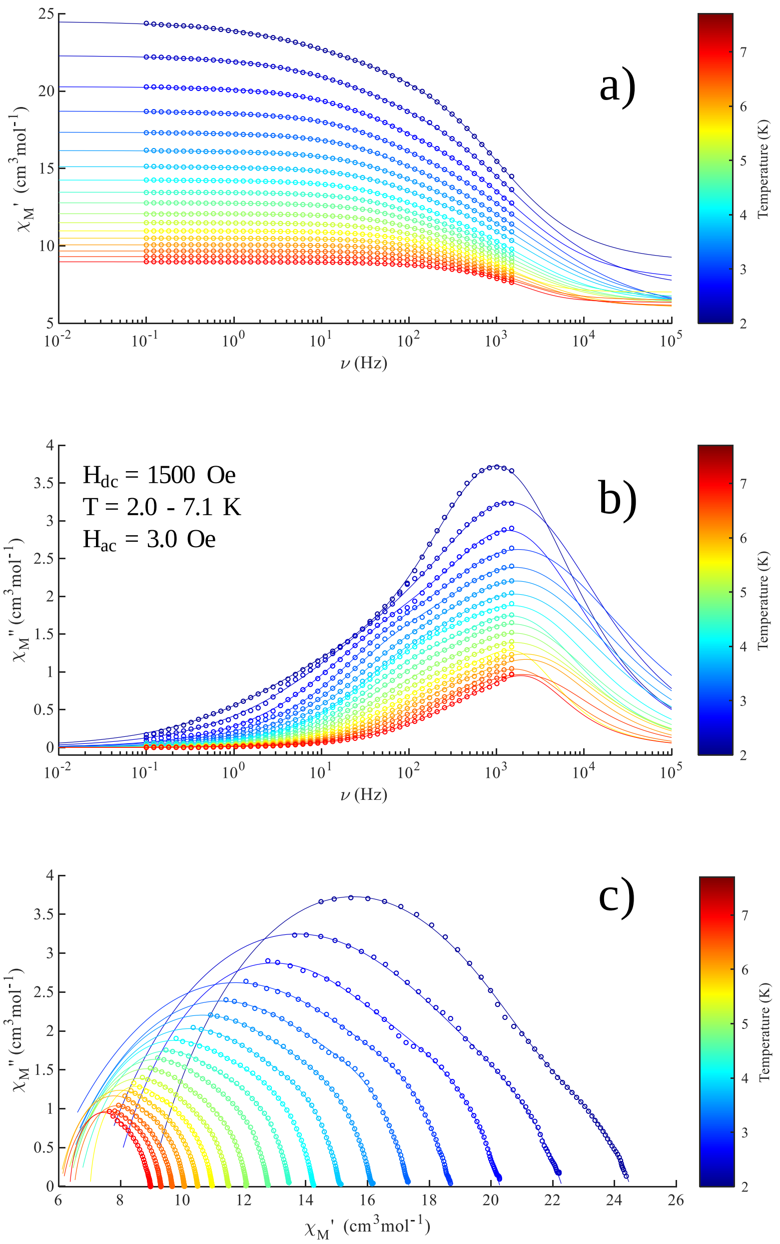

Figure S11. Temperature dependence of *ac* susceptibility a,b) (H_{ac}=3.0 Oe) and Cole-Cole plots(c) for **1** at indicated temperature and field. The solid lines represented the best fits according the generalized Debye model for two relaxation processes. (eq. 1, 2) see also **Figure S12**)

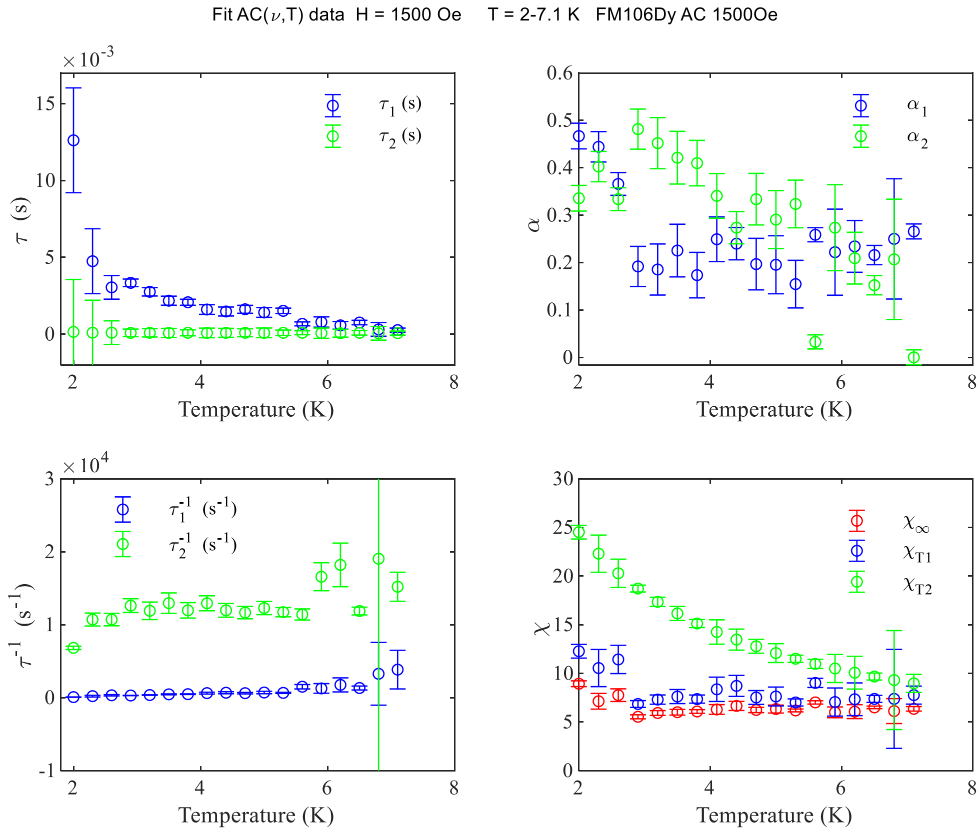

Figure S12. Graphical representation of variable parameters deduced from the best fits of the *ac* susceptibility of **1** collected under 1.5 kOe static field at deferent temperatures using the generalized Debye model for two relaxation processes. (See also **Figure S11**).

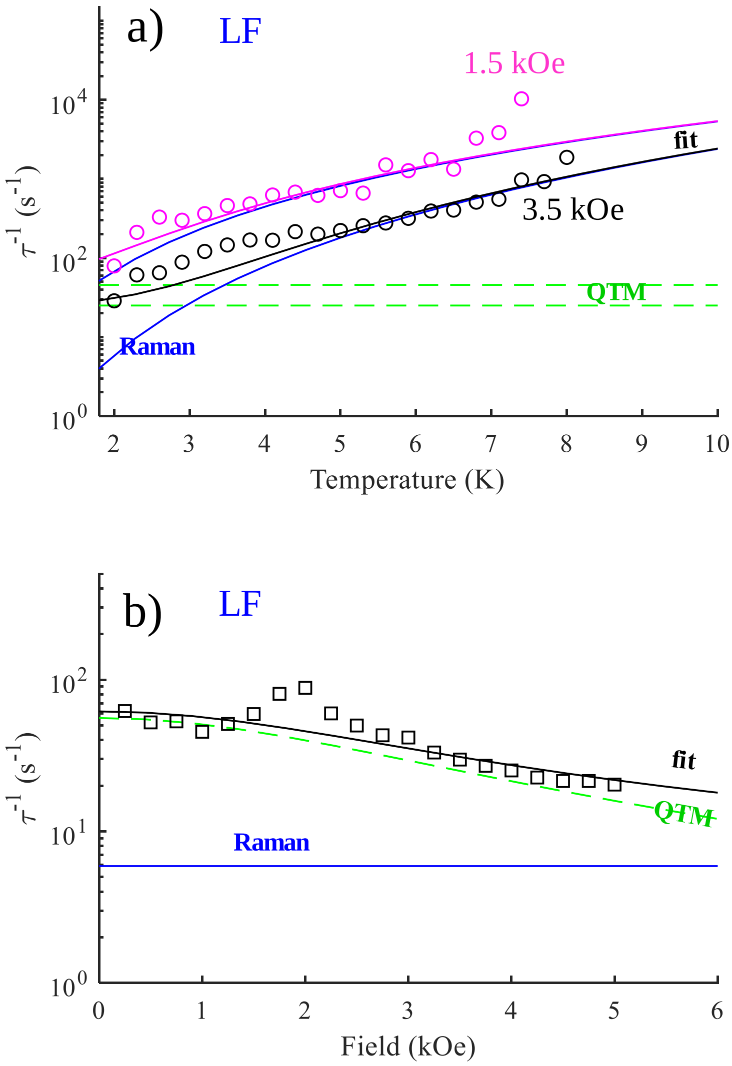

Figure S13. Temperature (a) and Field (b) dependence of relaxation time for Low Frequency process in **1**. The solid lines are the best fits with contribution of Raman and QTM.

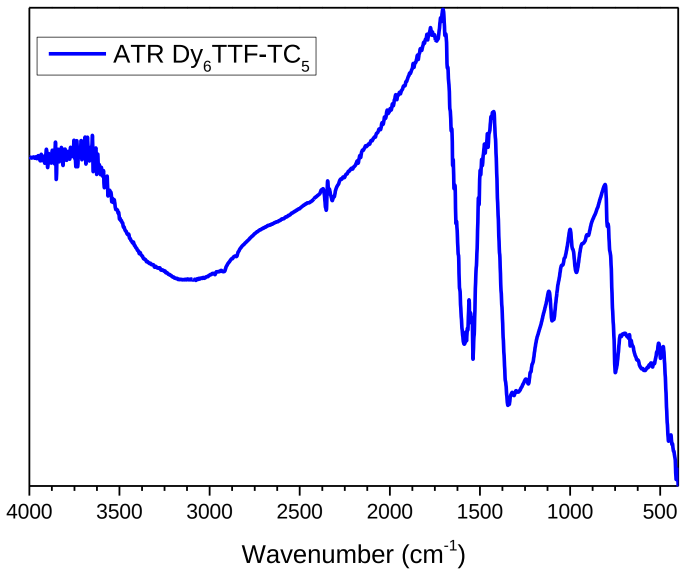

Figure S14. The ATR Spectrum of 1.

References

1 T. L. A. Nguyen, R. Demir-Cakan, T. Devic, M. Morcrette, T. Ahnfeldt, P. Auban-Senzier, N. Stock, A. M. Goncalves, Y. Filinchuk, J. M. Tarascon and G. Férey, *Inorg. Chem.*, 2010, **49**, 7135–7143.

2 Y. Han and Y. Song, *Inorg. Chem. Commun.*, 2015, **55**, 83–87.

3 Y. F. Han, M. Li, T. W. Wang, Y. Z. Li, Z. Shen, Y. Song and X. Z. You, *Inorg. Chem. Commun.*, 2008, **11**, 945–947.

4 Y. De Huang, P. Huo, M. Y. Shao, J. X. Yin, W. C. Shen, Q. Y. Zhu and J. Dai, *Inorg. Chem.*, 2014, **53**, 3480–3487.

5 S. Zhang, D. K. Panda, A. Yadav, W. Zhou and S. Saha, *Chem. Sci.*, 2021, **12**, 13379–13391.

6 S. S. Park, E. R. Hontz, L. Sun, C. H. Hendon, A. Walsh, T. Van Voorhis and M. Dincə, *J. Am. Chem. Soc.*, 2015, **137**, 1774–1777.

7 L. S. Xie, E. V. Alexandrov, G. Skorupskii, D. M. Proserpio and M. Dincă, *Chem. Sci.*, 2019, **10**, 8558–8565.

8 J. Castells-Gil, S. Mañas-Valero, I. J. Vitórica-Yrezábal, D. Ananias, J. Rocha, R. Santiago, S. T. Bromley, J. J. Baldoví, E. Coronado, M. Souto and G. Mínguez Espallargas, *Chem. - A Eur. J.*, 2019, **25**, 12636–12643.

9 J. Su, T. H. Hu, R. Murase, H. Y. Wang, D. M. D'Alessandro, M. Kurmoo and J. L. Zuo, *Inorg. Chem.*, 2019, **58**, 6, 3698–3706.

10 L. S. Xie and M. Dincă, *Isr. J. Chem.*, 2018, **58**, 1119–1122.

11 J. J. Hu, Y. G. Li, H. R. Wen, S. J. Liu, Y. Peng and C. M. Liu, *Dalt. Trans.*, 2021, **50**, 14714–14723.

12 J. Su, N. Xu, R. Murase, Z. Yang, D. M. D'Alessandro, J. Zuo and J. Zhu, *Angew. Chem.*, 2021, **133**, 4839–4845.

13 Z. R. Zhang, Z. H. Ren, C. Y. Luo, L. J. Ma, J. Dai and Q. Y. Zhu, *Inorg. Chem.*, 2023, **62**, 4672–4679.

14 J. Su, S. Yuan, Y. X. Cheng, Z. M. Yang and J. L. Zuo, *Chem. Sci.*, 2021, **12**, 14254–14259.

15 J. Liu, D. H. Zhang, B. Wang, Z. A. Nan, X. L. Cao, G. L. Li, W. Wang, Z. Zhuo, Z. X. Lu and Y. G. Huang, *J. Mol. Struct.*, 2023, **1292**, 136119.

16 F. Zhai, H. Li, D. Gui, C. Xia, Z. Chai and S. Wang, *Dalt. Trans.*, 2022, **12**, 16448–16452.

17 H. Y. Wang, J. Su, J. P. Ma, F. Yu, C. F. Leong, D. M. D'Alessandro, M. Kurmoo and J. L. Zuo, *Inorg. Chem.*, 2019, **58**, 8657–8664.

18 Z. H. Ren, Z. R. Zhang, L. J. Ma, C. Y. Luo, J. Dai and Q. Y. Zhu, *ACS Appl. Mater. Interfaces*, 2023, **15**, 6621–6630.

19 H. Y. Wang, J. Y. Ge, C. Hua, C. Q. Jiao, Y. Wu, C. F. Leong, D. M. D'Alessandro, T. Liu and J. L. Zuo, *Angew. Chemie - Int. Ed.*, 2017, **56**, 5465–5470.

20 M. A. Gordillo, P. A. Benavides, D. K. Panda and S. Saha, *ACS Appl. Mater. Interfaces*, 2020, **12**, 12955–12961.

21 M. A. Gordillo, P. A. Benavides, K. Spalding and S. Saha, *Front. Chem.*, 2021, **9**, 1–6.

22 F. Solano, P. Auban-Senzier, I. Olejniczak, B. Barszcz, T. Runka, P. Alemany, E. Canadell, N. Avarvari and N. Zigon, *Chem. - Eur. J.*, 2023, **29**, e202203138.